Supplementary document to

Ultra-programmable buckling-driven soft cellular mechanisms

S. Janbaz, F.S.L. Bobbert, M.J. Mirzaali, A.A. Zadpoor

Department of Biomechanical Engineering, Faculty of Mechanical, Maritime, and Materials Engineering, Delft University of Technology, Mekelweg 2, Delft 2628CD, The Netherlands

Materials and methods summary

For each type of unit cell, four parameters, i.e. ϕ, r, d, n, determined the shape of the voids and, thus, ligaments (details below). To create the 3D unit cells, 2D void shapes were projected onto the six external tangential planes from the three major mid-planes of a hollow sphere with outside and inside diameters of 20 and 12.5 mm (Figure S1a). The symmetric voids were then formed by loft cutting through the internal and external void shapes. To ensure that the dimensions of the generated ligaments were in the same range and that the integrity of the unit cells were preserved, the projected 2D voids on the surfaces of the corresponding cube were respectively scaled by 7.0, 7.5 or 8.0 for the circular, four-fold type I, and four-fold type II void geometries.

An advanced multi-material 3D printer (Stratasys Object 350 Connex3, US) working on the basis of jetting multiple UV-curable polymers was used to 3D print nine cellular structures with the three different void shapes and three different ratios of the mechanical properties of the corner parts to central parts (i.e. 0.5, 1, and 2). The more compliant material used for 3D printing of the corner or central parts was Agilus (Stratasys, US) while the stiffer material was a digital combination of Agilus and Vero Cyan (Stratasys, US). Vero (a hard polymer) (Stratasys, US) was used to print the end clamps. A soluble support material (SUP706, Stratasys, US) was used to preserve the details of the structures during the printing process. The cellular structures were first cleaned manually and were then soaked in a solution of 2% sodium hydroxide (NaOH) and 1% sodium metasilicate (Na2SiO3) in water for 2 hours to completely dissolve the support material. Fabrication of a single specimen takes about 16 hours and costs a few hundred Euros. Cellular structures were compressed with a strain rate of 1 mm/min using a Lloyd universal test bench (LR5K) equipped with a 100 N load cell. A digital camera (Sony A7R with a Sony FE 90 mm f/2.8 macro OSS lens) was used to capture the deformations of the specimens during the tests.

Computational models were built to study the instability behavior of the designed mechanical metamaterials under compression. A Neo-Hookean hyperplastic material model was used to describe the constitutive behavior of all materials. The material parameter (C_{10}) was determined according to the results of uniaxial tensile tests on base materials (details below). The instability modes were determined using an eigenvalue analysis and were then introduced for nonlinear analysis of the buckling and post-bucking behavior of the specimens. A nonlinear finite element solver (Abaqus Standard, ver. 6.14) was used for all simulations. Half-whole models were created for all the nine experimentally studied specimens and were discretized using ten-node hybrid tetrahedral elements (C3D10H). The nodes at the top and bottom surfaces of the specimens were constrained to satisfy the clamping conditions. A reference point was allowed to translate in the vertical direction. The onset of instability was determined by finding the maximum curvature at the start of the nonlinear phase in the stress-strain curves. The stiffness of the cellular structures was calculated using the data from the middle part of linear region in the corresponding stress-strain curve of each specimen.

Geometric design

The 2D patterns used to design the geometry of the voids were generated using a rotational vector previously described in [1]. Three selected combinations of parameters resulted in the circular $((\phi, r, d, n) = (0.45, 1.0, -, -))$, four-fold type I $((\phi, r, d, n) = (0.45, 0.7, +1, 4))$, and four-fold type II $(\phi, r, d, n) = (0.45, 0.8, -1, 4))$ voids symmetrically confined in a square with a length size of 2.5 mm. 2D void shapes were projected onto the six external tangential planes from the three major mid-planes of a hollow sphere with outside and inside diameters of 20 and 12.5 mm. The symmetric voids were then formed by cutting-loft through the internal and external void shapes forming a porous ball with 6 holes (Figure S1a). The projected 2D voids on the surfaces of the corresponding cube were respectively scaled up by 7.0, 7.5 and 8.0 times to create the *representative* unit cells with four-fold type II, circular, and four-fold type I void shapes. The selected projection ratios assured that the dimensions of the generated ligaments were similar and that the integrity of the buckliballs were preserved. The *translational* unit cell that could be repeated in different directions to create the cellular structure is somewhat different from the *representative* unit cells and is equal to the shared volume of the BCC assembly of nine unit-cells with a cube when the vertices of the cube are placed on the center of eight *representative* unit cells (Figure S1b). To study the effects of the material properties on the buckling behavior of cellular structures, the representative unit cells were segmented into corner and central parts using six two-by-two parallel cutting planes resulting in ligaments with lengths of 25% of the external diameter of the unit cells. All four combinations of flexible and stiff material properties were used for the corner and central parts of the representative unit cells. The lattice structures based on the BCC arrangement of the unit cells, with a lattice parameter of $a = 22.5\, mm$ and comprising $4 \times 4 \times 4$ unit cells were selected to numerically study the instability behavior of mechanical metamaterials. Finally, two rigid clamps were included on both parallel ends of the structures to facilitate the clamping of the specimens during uniaxial compression tests (Figure S1c).

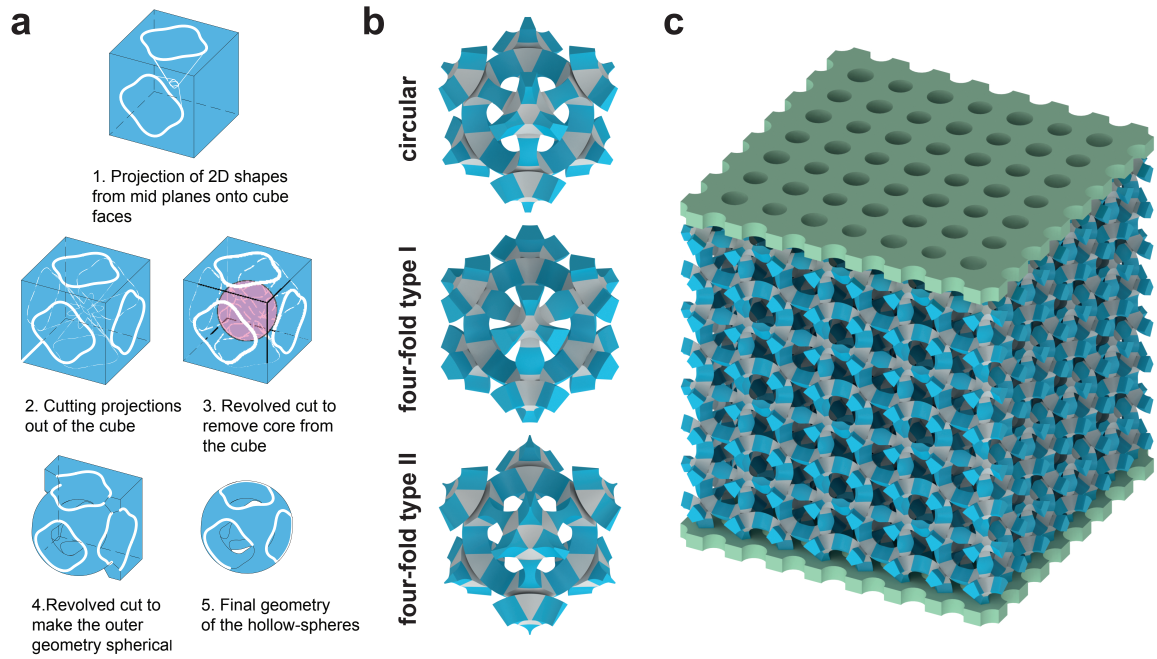

Figure S1. (a) Projection of 2D shapes to the six faces of a cube upon which the designs of the voids are based. (b) Circular, four-fold type I, and four-fold type II *translational* unit cells. The gray and blue elements represent the corner and central parts of the unit cells. (c) A four-fold type II specimen comprising $4 \times 4 \times 4$ unit cells and two rigid clamps at the top and bottom sides.

Mechanical properties of the base materials

We characterized the base (flexible and stiff) materials used for fabrication of the cellular structures. Strips (80 × 10 × 3 mm) of both types of materials were 3D printed with rigid end parts using a similar procedure as the one used for fabrication of multi-material cellular structures. Tensile tests under quasi-static condition were performed to measure the hyperelastic properties of the soft and stiff rubbers (Figure S2). The mean stress-strain curve of each group was used to evaluate the Neo-Hookean parameters (C_{10}) using the parameter estimation algorithm available in Abaqus, resulting in two values of $C_{10} = 115kPa$ and $C_{10} = 230kPa$ for the flexible and stiff polymers, respectively. SEM inspection of the flexible and stiff rubbers revealed no clear formation of void in the polymers. The materials were considered to be incompressible.

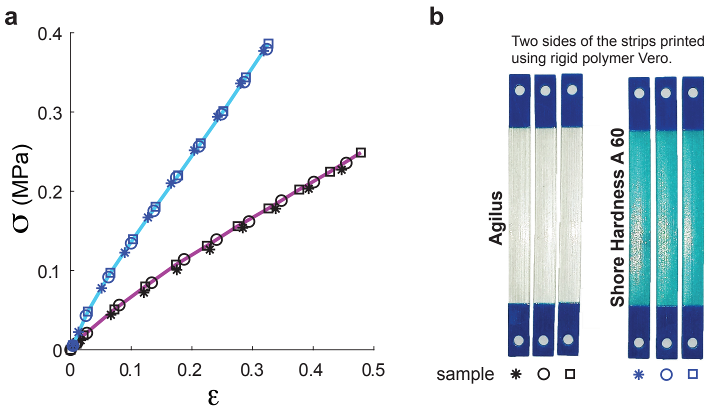

Figure S2. (a) The stress-strain curves obtained from tensile tests. (b) The tensile test strips (80 × 10 × 3 mm) with rigid end parts.

Computational models

As described in the summary of materials and methods, computational models were built to study the effects of geometrical design and material properties on the critical behavior of soft cellular structures. Some relatively small differences between the experimental observations and computational analyses were observed (Figure 1 and Figure S3). We performed a microscopic analysis to study the reason for those deviations and found out that these differences are most likely due to the geometrical imperfections created by the fabrication process (Figure S4). The differences in material properties caused by different UV exposures (time, orientation) may also influence the experimental results. Some of the micro- and macro-scale geometrical imperfections observed in the specimens are visualized in Figure S4. Studies on 3D printed hard materials have also shown deviations of experimental observations from computational results caused by manufacturing imperfections even for small strains [2].

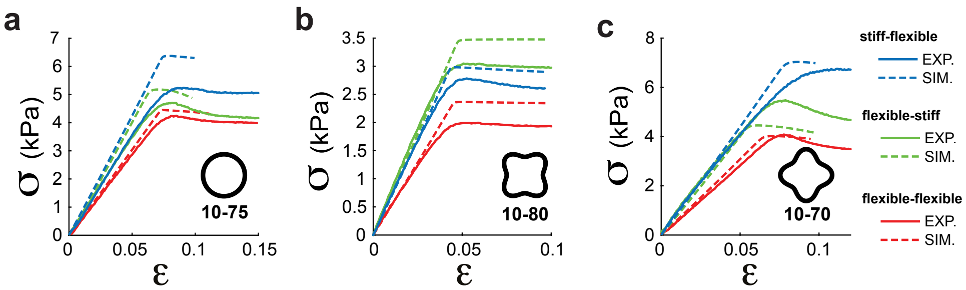

Figure S3. The experimental and computational stress-strain curves of (a) circular, (b) fourfold type I, and (c) four-fold type II specimens.

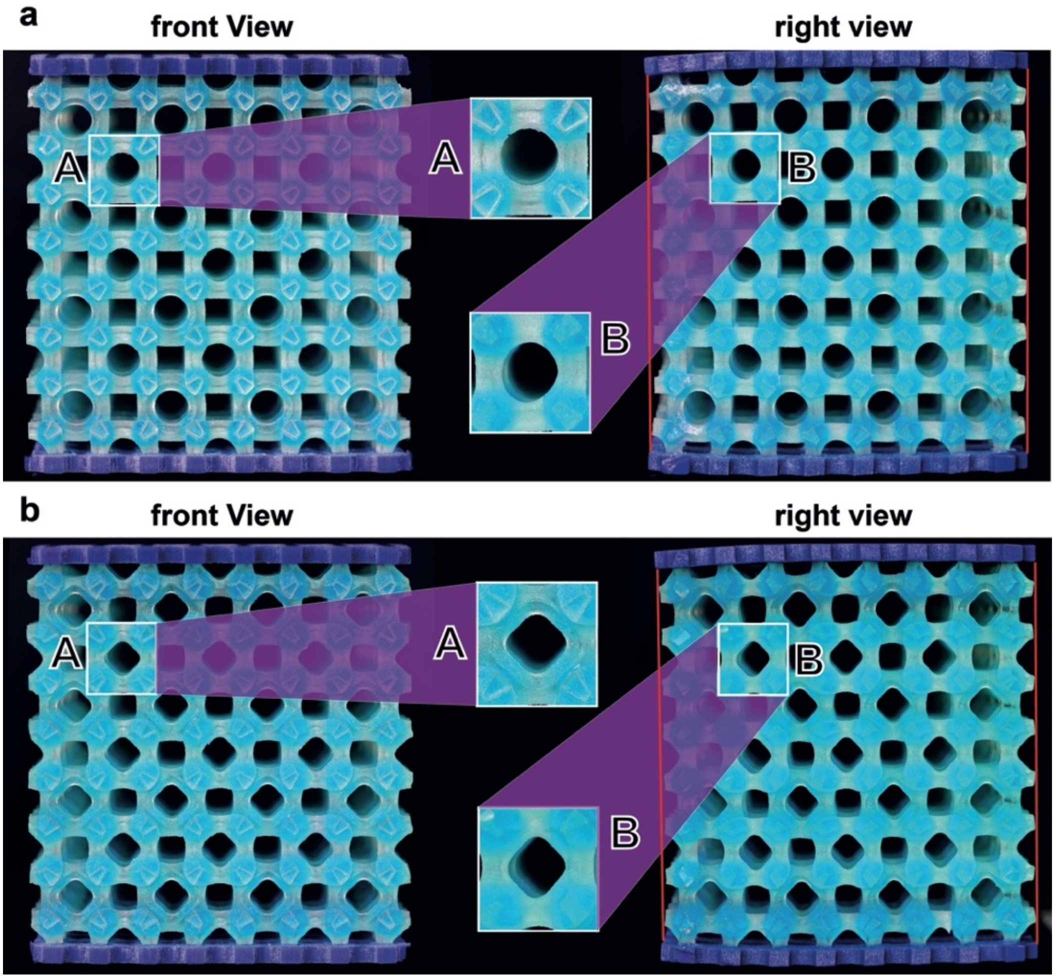

Figure S4. Microscopic and macroscopic geometrical imperfections were observed in the specimens produced using multi-material 3D printing. (a) The microscopic imperfections were manifested as deviations from the prescribed void shape. Macroscopically, a small deviation from straight line (to concavity) was observed in one of the faces of the specimen. (b) Similar macroscopic deviations are observed in four-fold type II specimens.

Experimental evidence for the predicted buckling modes

To study the buckling modes of actual 3D printed specimens, we fabricated 9 specimens with the projection ratios of 10-80, 10-75, and 10-75 based on the four-fold type I, four-fold type II, and circular unit cells, respectively. Combining flexible and stiff materials in the central and corner regions resulted in the emergence of a new instability (buckling) mode, namely double-side buckling (Figures S5). The cellular materials studied to date usually exhibit one of the two instability modes of side buckling or symmetric compaction. One of the reasons has been that most of such metamaterials have been studied in 2D, where double-side buckling is not possible. However, double-side buckling has not been observed even in a handful of 3D designs that can be found in the literature. Our computational models clearly showed that not only the geometrical design parameters such as the type of the unit cell and porosity but also the distribution of the material properties influence the type of the instability mode (Figure 2d). That is because both types of design parameters could substantially change the distribution of the strains in each of the 12 complaint links making up the unit cells (Figure 2e).

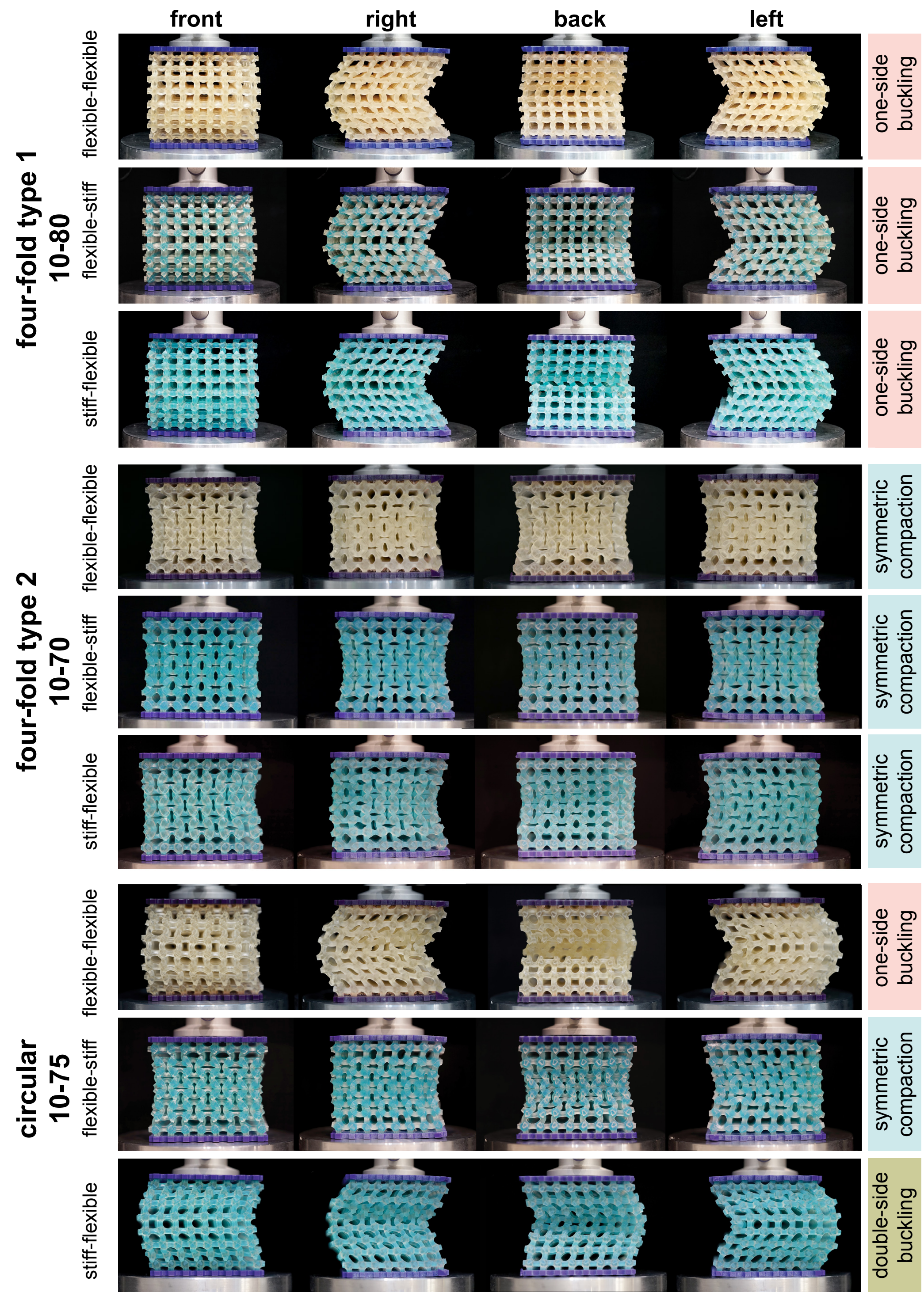

Figure S5. The different views of the first instability (actuation) modes observed experimentally. There are three types of instability modes including symmetric compaction, side-buckling, and double-side buckling. The nominal dimensions of all specimens were 90×90×90 mm. Photographs were taken at 15 mm axial displacement for the fourfold type I geometries and at 20 mm axial displacement for both other geometries.

Activation of higher instability modes

Computational analysis revealed that the third instability mode for the cellular structures based on the four-fold type I voids is a rotational (twisting) mode regardless of the spatial distribution of the mechanical properties. The eigenvalue associated with this instability mode (according to linear buckling analysis) was < 2% higher than that of the first eigenvalue. To switch the order of instability modes, the post-buckling shape of the third mode was introduced as an imperfection modifying the geometry of the cellular structures. Two imperfection amplitudes (4 and 8) from the linear buckling analysis performed for a specific cellular structure (10-80, flexible-flexible, four-fold type I) were used to create the half-whole models that were then exported as geometry files, mirrored, and assembled using Blender (version 2.77) to create the geometry of full models. Similar to the previous specimens, two rigid clamps were included at the top and bottom of these specimens. To visualize the rotation of the specimens during compression, two lightweight rings (placed at the mid-section of the specimens) were 3D printed using polylactic acid (PLA). The cellular structures were cleaned and compressed using an Instron testing machine (5500R equipped with a 1 kN load cell). The tests were performed both with and without the lightweight rings to ensure the addition of the rings does not significantly influence the results. Computational analysis using four different imperfection amplitudes (0.5, 1, 4, and 8) was used to evaluate the effects of the spatial distribution of the material properties, projection ratio, and the imperfection size on the characteristic curve of the cellular structures. Four reference points at the corners of the bottom side of the half-whole models were used to calculate the rotation of the mid-section of the full models when compressed.

Demonstration of the potential applications in robotics

To demonstrate some of the potential applications of the proposed concepts in robotics, we performed three experiments in which our soft mechanisms were used as a force switch, as kinematic (position/velocity) controllers, and as a pick and place grasping mechanism.

A raw egg was placed between the fixed compression plate and the free end of a cellular structure (four-fold type II, $(\phi, r, d, n) = (0.45, 0.8, -1, 4)$) (supplementary video 2, Figure 4a). The top side of the soft mechanical material was clamped to the moving compression plate. To avoid hard contact between the egg and the contact plates, two 1 mm thick semi-soft PVC plates were placed between the contact surfaces of the egg and the compression setup. To minimize possible bending moments, the egg was placed at the middle area of the soft mechanisms. The cellular structure was compressed after touching the egg for up to 25 mm (compression rate = 20 mm/min).

Using imperfections with different amplitudes (1 and 12), cellular solids (four-fold type I ($(\phi, r, d, n) = (0.45, 0.7, +1, 4)$, projection ratio: 10-70) were pre-disposed to activate their third modes of instability (Figure 3) and were used as kinematic (position/velocity) controllers. Two rigid arms were fixed to two rings placed at the middle part of the soft mechanisms in order to push two table tennis balls when the soft mechanisms were compressed (supplementary video 3, Figure 4b). Both structures were compressed at the same time using a high compression rate of 500 mm/min. A MATLAB code was used to estimate the rotation angle of the rigid arms using a number of recorded images.

A soft cellular structure (four-fold type I $(\phi, r, d, n) = (0.45, 0.7, +1, 4)$, projection ratio 10-70, imperfection amplitude: 12) was pre-disposed to activate its third mode of instability and was used as a part of a pick and place grasping mechanism. The cellular structure was constrained between two clamps that were linked together using four linear ratchet and pawl mechanisms (Figure S6). A gear ring at the middle part of the cellular structure was used for locking the end-effector into the picked objects with the first push. Further compression unlocked the ratchet and pawl mechanisms, thereby releasing the grasped object. A universal robotic arm (Universal Robots, UR5, Denmark) was programmed to perform a pick and place task (supplementary video 4, Figure 4c) that visualized the function of the mechanism.

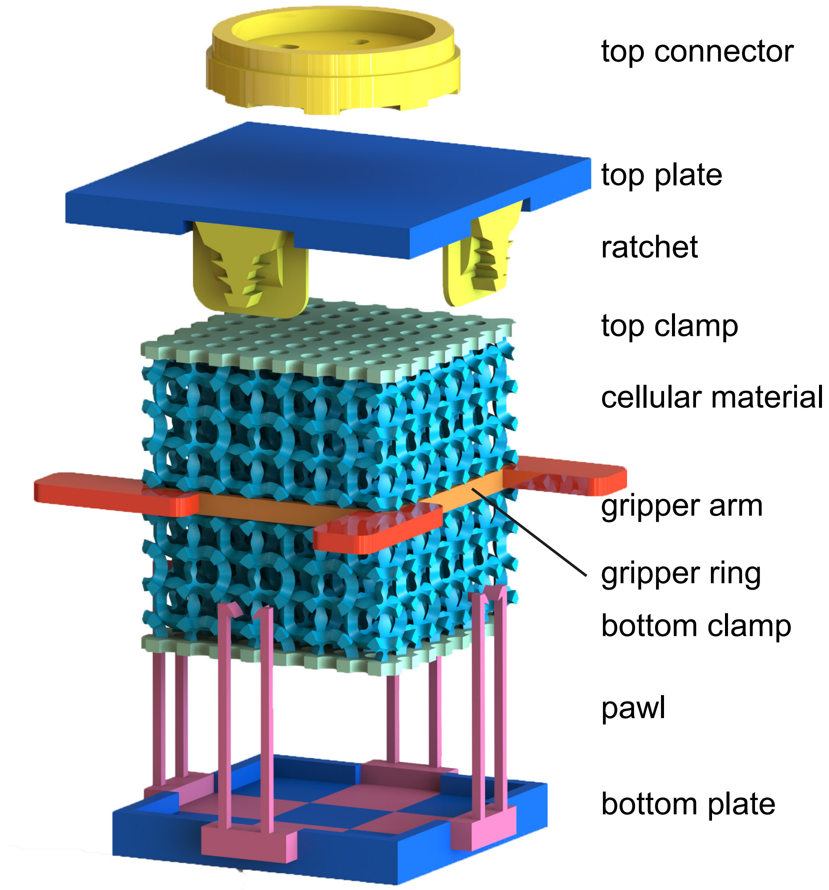

Figure S6. The components of the pick and place grasping mechanism. Four ratchet and pawl mechanisms enable the locking and unlocking of this rotational grasper.

Miniaturization

To evaluate the feasibility of miniaturizing the soft cellular mechanisms proposed here, we fabricated a number of specimens with gradually decreasing sizes using three different 3D printing techniques. At the macroscale, we fabricated 5 new specimens using the same technology used for the fabrication of the specimens shown in Figures S4-S5 (*i.e.*, Stratasys Object 350 Connex3, US). The specimens included the multi-material designs 1, 3, and 5 (project ratio: 10-75, flexible-stiff, circular voids, the number of unit cells: $3 \times 3 \times 3$) and single-material designs 4 and 5 (projection ratio: 10-75, stiff-stiff, circular voids, imperfection amplitude: 8 from the mode 4 of buckling) (Figure 5a). The flexible material was Agilus and the stiff material was a digital combination of Agilus and VeroMagenta. The size of the specimens could be decreased by up to 5 times using this technology. In order to proceed one step forward and further miniaturize the geometry of the specimens, we used stereolithography (layer thickness: 50 μm, Form 2, Formlabs, US) and a photocurable resin (Flexible, V2 (FLFLGR02), Formlabs, US) to manufacture a number of specimens (projection ratio: 10-75, single-material, circular voids, imperfection amplitude: 8 from the mode 4 of buckling) that were pre-disposed to activate their rotational mode of buckling (imperfection amplitude: 8 from the buckling mode 4). The specimens are shown in Figure 5b. The sizes of the specimens fabricated using stereolithography were up to 14 times smaller than the original specimens shown in Figure S4-S5. Finally, we used the two-photon polymerization technique (Photonic Professional GT, Nanoscribe GmbH, Germany) together with an acrylate-based polymer resin (IP-S, Nanoscribe GmbH) to fabricate cellular structures (four-fold type I, $(\phi, r, d, n) = (0.45, 0.7, +1, 4)$, projection ratio: 10-80, imperfection amplitude = 8 from the buckling mode

3) that was up to 180 times smaller than the specimens shown in Figures S4-S5. A 25x objective with an NA of 1.4 was used to deliver a nominal laser power of 20 mW at a writing speed of 100 mm/s. The polymerized structure was developed in PGMEA for 25 minutes, cleaned in isopropanol for 5 minutes, and finally blow dried. A scanning electron microscope (SEM, JSM-IT100, JEOL, Japan) was used to image the specimen (Figure 5c). Prior to SEM imaging, the specimen was gold-coated using a sputter coater (JFC-1300, JEOL, Japan) to make it conductive.

Simultaneous activation of multiple buckling modes

In order to predict the feasibility of activating multiple modes of buckling simultaneously, we performed computational modeling to predict the buckling modes of a cellular structure with a higher aspect ratio than those of the previously considered specimens (*i.e.*, four-fold type I $(\phi, r, d, n) = (0.45, 0.7, +1, 4)$, projection ratio: 10-70, $3 \times 3 \times 6$ unit cells, scale = 50%, Figure 5d). The deformations corresponding to the buckling modes 3 (*i.e.*, rotation) and 4 (*i.e.*, a wavy-shaped deformation pattern) were then scaled (imperfection amplitudes = 8 and 4, respectively) and added to each other to create a geometrical imperfection that was then used to pre-dispose the cellular structure (Figure 5d). Subsequently, we fabricated the pre-disposed design using the same multi-material 3D printer (Polyjet technology, Stratasys Object 350 Connex3, US) that was used for the fabrication of the specimens shown in Figures S4-S5. A digital material (combination of Agilus and VeroMagenta) was selected for the fabrication of this specimen. Our experiments clearly showed that the specimen designed using this approach deforms under a combination of the buckling modes 3 and 4 (Figure 5d) which confirms that the deformations resulting from multiple modes of buckling could be combined with each other to program very complex deformation patterns into the soft mechanisms proposed here.

References

[1] Janbaz S, Weinans H, Zadpoor AA. Geometry-based control of instability patterns in cellular soft matter. RSC Adv 2016;6:20431-6.
[2] Campoli G, Borleffs MS, Yavari SA, Wauthle R, Weinans H, Zadpoor AA. Mechanical properties of open-cell metallic biomaterials manufactured using additive manufacturing. Mater Design 2013;49:957-65.